

# RSC Advances



This is an *Accepted Manuscript*, which has been through the Royal Society of Chemistry peer review process and has been accepted for publication.

*Accepted Manuscripts* are published online shortly after acceptance, before technical editing, formatting and proof reading. Using this free service, authors can make their results available to the community, in citable form, before we publish the edited article. This *Accepted Manuscript* will be replaced by the edited, formatted and paginated article as soon as this is available.

You can find more information about *Accepted Manuscripts* in the [Information for Authors](#).

Please note that technical editing may introduce minor changes to the text and/or graphics, which may alter content. The journal's standard [Terms & Conditions](#) and the [Ethical guidelines](#) still apply. In no event shall the Royal Society of Chemistry be held responsible for any errors or omissions in this *Accepted Manuscript* or any consequences arising from the use of any information it contains.

## High thermal radiation of Ca-doped lanthanum chromite

Cite this: DOI: 10.1039/x0xx00000x

Yi Lu,<sup>a</sup> Zhenggang Fang,<sup>a</sup> Chunhua Lu,<sup>a†</sup> Ling Wei,<sup>a</sup> Yaru Ni,<sup>a</sup> Zhongzi Xu<sup>\*†</sup> and Shunyan Tao<sup>b</sup>

Received 00th January 2012,  
Accepted 00th January 2012

### Abstract

Calcium-doped lanthanum chromite,  $\text{La}_{1-x}\text{Ca}_x\text{CrO}_3$ , was prepared using a solid-state reaction method, and the effect of varying the Ca content ( $0 \leq x \leq 0.5$ ) was investigated in relation to its crystalline structure, surface morphology, solar absorption and thermal radiation. This found that the crystalline structure is slightly distorted by  $\text{Ca}^{2+}$  doping, with an accompanying increase in the valence state of Cr ions and oxygen vacancies enhancing both the solar absorption and thermal emittance. Overall, the  $\text{La}_{1-x}\text{Ca}_x\text{CrO}_3$  system displays relatively high thermal radiation properties, with an optimal composition of  $\text{La}_{0.5}\text{Ca}_{0.5}\text{CrO}_3$  exhibiting a solar absorption of 95 % and a thermal emittance of 0.94. When used as a light absorber coupled to a thermoelectric module this proved capable of generating electricity and hot water, thereby demonstrating the suitability of this energy-saving material for use in solar thermal radiation applications.

DOI: 10.1039/x0xx00000x

[www.rsc.org/](http://www.rsc.org/)

### Introduction

The continued depletion of fossil fuel reserves over recent years has seen non-conventional energy resources playing a more prominent role in everyday life; and as such, there has been increasing interest in solar energy given that it represents a virtually inexhaustible energy resource. Existing technology for converting solar energy to more usable forms can be divided into two distinct categories: solar thermal conversion,<sup>1-6</sup> which produces thermal energy, and photovoltaic (PV) conversion,<sup>7-9</sup> which produces electrical energy. Of these, solar thermal has become the more popular approach to solar energy conversion, being in concentrating solar power (CSP) systems that are expected (with appropriate support) to provide 10 % of the world's electricity by 2050.

The efficiency of solar thermal power depends on the solar absorber materials, which are typically classified as selective or non-selective depending on their absorptance to emittance ratio. Selective absorber materials such as carbide and boride ceramics<sup>10-15</sup> offer excellent solar thermal conversion thanks to a high solar absorption and low emissivity, whereas the outstanding radiative heat transfer of non-selective absorber materials is can be attributed to a high solar absorption and emissivity.<sup>6-18</sup> High temperature emissivity measurements, however, have typically been carried out in a vacuum rather than an actual working environment in the presence of air; and as such, are not really relevant to absorbers that are currently subjected to extreme variations in operating temperature from more than 500 °C to less than 0 °C at night. A few excellent reviews of

mid-temperature (100–400 °C) and high-temperature (400–700 °C) absorber materials have been published over the years,<sup>19,20</sup> but a survey of these reveals that only a few non-selective coatings have been developed that are suitable for high-temperature applications. Adding to the problem is the fact that these absorbers also need to meet certain requirements with regards to corrosion resistance and an ability to withstand severe abrasion by sand and dust. Thus, the last few years have seen high-temperature absorbers being increasingly sought after as a means of improving solar thermal conversion efficiency.

Ceramics, which are amongst the cheapest and most versatile of engineering materials, can offer the necessary combination of good thermo-physical properties, high workability, and stability at high temperature in either oxidizing or reducing atmospheres. As an alternative ceramic material, which has been used successfully as a cathode material,<sup>21-24</sup> alkaline-earth doped  $\text{LaCrO}_3$  offers high thermal and chemical stability under an oxidizing atmosphere, as well as the ability to withstand high temperatures.<sup>25-28</sup> For example, Hilpert studied  $\text{LaCrO}_3$ -based interconnects exposed to oxidizing and reducing atmospheres and found that the oxygen non-stoichiometry of doped chromites has a large impact on the nature of the dopants and the defect structure of the chromites.<sup>24</sup> Aliovalent doping also affects the properties of a material by manipulating its oxygen vacancy concentration.<sup>29-31</sup> Using this, Khomchenko et al. have demonstrated that the ferroelectric and magnetic properties of aliovalent-doped  $\text{Bi}_{0.95}\text{Ca}_{0.05}\text{Fe}_{1-y}\text{B}_y\text{O}_3$  ( $B = \text{Ti}$  and  $\text{Mn}$ ;  $y = 0, 0.05, 0.1$ ) perovskites can be tailored through an elimination of oxygen

vacancies by *B*-site substitution.<sup>32</sup> It is also worth noting that impurities and the addition of free carriers caused calcium-doped LaCrO<sub>3</sub> to become a p-type semiconductor,<sup>33-35</sup> which has a significant effect on its spectral properties. However, there have as yet been few reports pertaining to the spectral absorption properties of the La<sub>1-x</sub>Ca<sub>x</sub>CrO<sub>3</sub> system.

We therefore herein report on the preparation of a series of La<sub>1-x</sub>Ca<sub>x</sub>CrO<sub>3</sub> oxides by a solid-state reaction method, which was monitored through thermogravimetric and differential thermal analysis. The effect of Ca doping on the solar absorbance and thermal emittance is also explored, along with any associated change in the crystal structure or surface morphology, with a view to the material's potential application as a solar absorber material.

## Experimental

### Materials and methods

Samples of La<sub>1-x</sub>Ca<sub>x</sub>CrO<sub>3</sub> ( $0 \leq x \leq 0.5$ ) were synthesized by means of a standard solid-state reaction. For this, analytical-grade dry powders of La<sub>2</sub>O<sub>3</sub>, CaCO<sub>3</sub>, and Cr<sub>2</sub>O<sub>3</sub> were first mixed to an appropriate weight ratio, as calculated from the stoichiometric composition, and then ball milled with ethanol. The resulting mixtures were dried, placed in a crucible, and then calcined overnight at 900 °C. The calcined powders were subsequently reground, mixed with polyvinyl alcohol, and then pressed at 10 MPa into discs measuring 60 mm in diameter and 3 mm in thickness. Finally, these discs were sintered at 1400 °C for 10 h at a rate of 3 °C/min, giving a final sample weight of ~15 g. The resulting La<sub>1-x</sub>Ca<sub>x</sub>CrO<sub>3</sub> samples were named as LC0, LC1, LC2, LC3, LC4 and LC5 according to the amount of Ca dopant added ( $x=0, 0.1, 0.2, 0.3, 0.4, 0.5$ ).

### Characterization

The calcination of the ceramic was assessed through a combination of thermogravimetric analysis and differential scanning calorimetry (TGA-DSC, NETZSCH STA 449C) in order to measure the weight loss, the change in thermal properties and the temperature of reaction. Heating and cooling rates were maintained at 20 °C/min, with a maximum temperature of 1300 °C under an air atmosphere being used throughout. A powder X-ray diffraction (XRD) system (ARL X'TRA, Thermo Scientific) with a Cu *K*<sub>α</sub> radiation source ( $\lambda = 0.15406$  nm) was used to characterize the crystalline structure and identify the dominant phase present in the powders after calcination. The Rietveld refinement analysis was performed with General Structure Analysis System (GSAS) EXPGUI.<sup>36, 37</sup> The surface morphology of the samples was observed directly by scanning electron microscopy (SEM; SU8010, Hitachi) and the surface roughness was obtained by 3D Measure Laser Microscope (OLS4000, Japan). The thermal expansion coefficient (TEC) between room temperature and 500 °C was measured using an RPZ-01 dilatometer (Luoyang, China) at a heating rate of 5 °C min<sup>-1</sup>.

The composition of the samples was determined from Fourier transform infrared reflection spectra obtained with a Spectrum 400-FTIR (FT-IR, Frontier, PerkinElmer LLC) using the KBr pellet technique. Each spectrum represents an average of 32 scans obtained at ambient temperature in a wavelength range of 4000 to 400 cm<sup>-1</sup>. The surface composition was analyzed by X-ray photoelectron spectroscopy (XPS), using a scanning XPS microprobe (PHI5000 VersaProbe, ULVAC-PHI). A carbon contaminant (C1s = 284.6 eV) was used to calibrate all binding energy data, and the XPS spectrum was fitted by XPSpeak software. Reflectance spectra in the 0.2–2.5 μm wavelength range were measured using a UV–vis–NIR spectrophotometer (UVPC measurement software, Shimadzu; Varian Cary 5000, Varian), with BaSO<sub>4</sub> as the reflectance sample. The diffused spectra in the 2.5–15 μm wavelength range were obtained with FT-IR spectrometer (Frontier, PerkinElmer LLC) equipped with a gold-coated integrating sphere and a heating accessory.

With reflection measurement methods the emittance (absorptance) is obtained indirectly from the measured reflectance based on the relation for opaque materials,  $\epsilon = \alpha = 1 - R$ ;  $\epsilon$ ,  $\alpha$ , and  $R$  being the emittance, absorptance, and reflectance, respectively. The optical absorbance and thermal emissivity can be derived from the reflectance spectrum according to Eq. (1) and Eq. (2), respectively.<sup>38</sup>

$$\alpha_s = \frac{\int_{0.3\mu\text{m}}^{2.5\mu\text{m}} [1 - R(\lambda)] P_{SUN}(\lambda) d\lambda}{\int_{0.3\mu\text{m}}^{2.5\mu\text{m}} P_{SUN}(\lambda) d\lambda} \quad (1)$$

$$\epsilon_T = \frac{\int_{2.5\mu\text{m}}^{15\mu\text{m}} [1 - R(\lambda)] P_B(\lambda) d\lambda}{\int_{2.5\mu\text{m}}^{15\mu\text{m}} P_B(\lambda) d\lambda} \quad (2)$$

Here  $\lambda$  is the wavelength;  $R(\lambda)$  is the reflectance;  $P_{Sun}(\lambda)$  refers to the normal solar irradiance at wavelength  $\lambda$ , which is defined according to ISO standard 9845-1 (1992), AM 1.5; and  $P_B(\lambda)$  is given by Planck's law, which is calculated at 373.15 K according to Eq. (3):<sup>39</sup>

$$P_B(\lambda) = \frac{C_1}{\lambda^5 [\exp(C_2 / \lambda T) - 1]} \quad (3)$$

where  $C_1 = 3.743 \times 10^{-16}$  W·m<sup>2</sup>,  $C_2 = 1.4387 \times 10^{-2}$  m·K, and  $T$  is the absolute temperature.

Photo-thermal measurements were conducted using a solar simulator (model 94043A, 4×4 inch source diameter, Newport) fitted with an AM1.5 direct filter as the light source. The optical power density of the incident light concentrated by the Fresnel lens was measured by a hand-held optical power/energy meter (model 1918-R, Newport) equipped with a thermopile detector (Model 818P-020-12, Newport). Thermal radiation pictures of the samples under different intensities of solar radiation were obtained by FLIR cameras (Automation &

Science). For electrical measurements, a thermoelectric generator module (TEG1-127-1.0-2.0, Thermonamic Electronics Corp., Ltd., China) was attached between the ceramic absorber and a custom-made water cooler using thermally conductive adhesives. The current-voltage curves were then measured with a computer-controlled sourcemeter (Keithley 2440 5A).

## Results and discussion

### TG-DSC analysis

The thermogravimetric (TG) and differential scanning calorimetry (DSC) curves obtained for  $\text{La}_{1-x}\text{Ca}_x\text{CrO}_3$  ( $x=0, 0.2, 0.4$ ) sintered in an air atmosphere are shown in Fig. 1a and 1b. By combining these TG/DSC results with the XRD data in Fig. 1c, the process of synthesis can be divided into six separate stages. In Stage I, which ranges from room temperature to 300 °C, the slight mass loss evident in Fig. 1a is indicative of the loss of surface water. In Fig. 1b, the three endotherms at 338, 500 and 720 °C correspond to the decomposition of oxides. This is attributable to the fact that  $\text{La}_2\text{O}_3$  is mostly converted to  $\text{La}(\text{OH})_3$  during ball milling, and is then decomposed to  $\text{LaOOH}$  when heated to between 300 and 500 °C in Stage II. At the same time,  $\text{La}_2\text{O}_3$  also reacts with  $\text{CO}_2$  to form  $\text{La}_2(\text{CO}_3)_3$ , which decomposes to  $\text{La}_2\text{O}_2\text{CO}_3$  at a temperature between 500 and 720 °C in Stage III. At temperatures greater than 720 °C,  $\text{La}_2\text{O}_2\text{CO}_3$  decomposes to  $\text{La}_2\text{O}_3$ , which then reacts with  $\text{Cr}_2\text{O}_3$  in Stage IV.<sup>40</sup> The weight loss prior to 650 °C is mainly attributed to the change of  $\text{La}(\text{OH})_3$ , whereas the loss after 650 °C can be attributed to the known decomposition of  $\text{CaCO}_3$ .<sup>41</sup> Finally, the endothermic peak evident at 1080 °C in Stage V is validated by the XRD data in Fig. 1c as being associated with the formation of an  $\text{ABO}_3$ -type perovskite oxide, which can be described by the following reaction formula, Eq.(4)–Eq.(9):

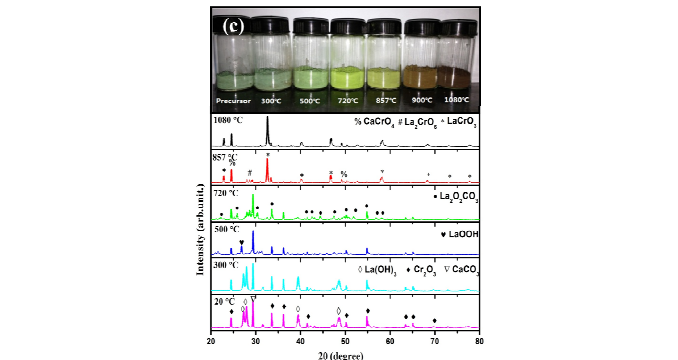
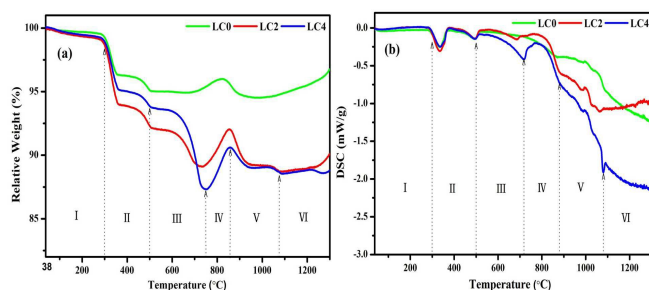
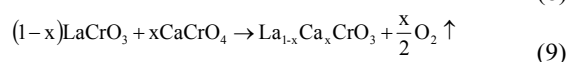
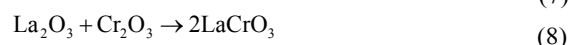
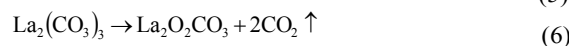


**Fig.1** TG/DSC curves of  $\text{La}_{1-x}\text{Ca}_x\text{CrO}_3$  (where  $x=0, 0.2, \text{ and } 0.4$ ) in air: (a) thermogravimetric curves, (b) differential scanning calorimetry curves, (c) XRD spectra of precursor oxides sintered at different temperatures.

### Structure and morphology

Structural distortion of the crystal lattice is known to vary with an increasing amount of  $\text{Ca}^{2+}$  dopant, with the degree of distortion being quantified by a tolerance factor ( $t$ ) that describes the geometric distortion of  $\text{ABO}_3$ -type perovskite as:

$$t = \frac{(r_A + r_O)}{\sqrt{2}(r_B + r_O)} \quad (10)$$

where  $r_A$ ,  $r_B$ , and  $r_O$  are the ionic radii of the ions. Since the ionic radius of atoms in the crystal structure also varies with changes in their coordination number or valence,  $t$  was calculated using the coordination numbers of A-site ions ( $\text{La}^{3+}$ , 1.061 Å;  $\text{Ca}^{2+}$ , 0.99 Å), Cr ions (0.52 Å), and O ions (1.40 Å, 6-fold coordinated) of 12, 6, and 6, respectively. The calculated values for the tolerance factor of the  $\text{La}_{1-x}\text{Ca}_x\text{CrO}_3$  ( $0 \leq x \leq 0.5$ ) samples range from 0.906 to 0.894; and as the  $t$  value of a perovskite structure typically lies between 0.75 and 1.1, this confirms that Ca-doped lanthanum chromites still retain an  $\text{ABO}_3$  perovskite structure.

Figure 2(a) shows the XRD spectra of the  $\text{La}_{1-x}\text{Ca}_x\text{CrO}_3$  ( $0 \leq x \leq 0.5$ ) samples sintered at 1400 °C for 10 h, in which the gradual shift in the main diffraction peaks toward a higher diffraction angle indicates a reduction in the crystal volume, and means that  $\text{Ca}^{2+}$  had already begun to substitute for  $\text{La}^{3+}$  and reduce the interplanar distance of the  $\text{LaCrO}_3$  lattice.<sup>42, 43</sup> Refinements were performed based on the following structures:  $\text{LaCrO}_3$  (ICSD 59595),  $\text{La}_{0.9}\text{Ca}_{0.1}\text{CrO}_3$  (ICSD 81985),  $\text{La}_{0.8}\text{Ca}_{0.2}\text{CrO}_3$  (ICSD 81989), and  $\text{La}_{0.7}\text{Ca}_{0.3}\text{CrO}_3$  (ICSD 81990), and the profile was fitted using pseudo-Voigt functions to fit the lattice and profile parameters GU, GV, GW, LX, and LY. The XRD pattern of  $\text{LaCrO}_3$  was selected for Rietveld fitting in Fig. 2(b), which shows the typical best fit that was observed and calculated, the difference in the diffraction profiles of the powders, and the expected Bragg reflections. The Rietveld refinements for  $\text{La}_{1-x}\text{Ca}_x\text{CrO}_3$  ( $0.1 \leq x \leq 0.5$ ) are shown in supplementary materials (Fig.S1). These results identified an orthorhombic structure with a  $Pnma$  space group at room temperature, and at all compositions. The refined

lattice parameters and unit cell volume obtained through structural refinements of the samples are shown in Tab.1, which reveals an obvious variation in both between different samples. For example, the lattice parameters ( $a$ ,  $b$ ,  $c$ ) and unit cell volume decrease with an increasing concentration of  $\text{Ca}^{2+}$  substituting for  $\text{La}^{3+}$  in  $\text{LaCrO}_3$  that can be attributed to the smaller ionic radii of  $\text{Ca}^{2+}$  ions. Aliovalent doping, however, can also generate oxygen vacancies and cause a transition in the ions valence state. This means that owing to the effects of charge compensation, trivalent chromium ions in oxides will convert to either a tetravalent or hexavalent form that will affect the angle and distance of  $\text{Cr}^{3+}\text{-O-Cr}^{4+}$  bonds. This, in turn, may have an effect on the absorption properties.

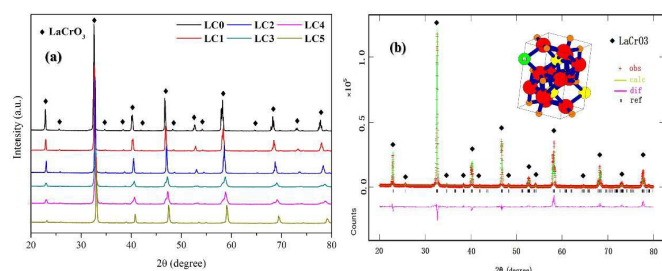


**Fig.2** (a) XRD patterns of  $\text{La}_{1-x}\text{Ca}_x\text{CrO}_3$  ( $0 \leq x \leq 0.5$ ) powders. Inset schematic is of the crystal structure of  $\text{LaCrO}_3$ . (b) Rietveld refinements (line) of the observed XRD patterns (+) for  $\text{LaCrO}_3$ . Vertical bars below each pattern show the position of all possible reflection peaks, while the lowest curve depicts the difference between the observed and calculated intensity.

**Table 1** Summary of the results of the least-squares refinements of the XRD diffraction data collected from  $\text{La}_{1-x}\text{Ca}_x\text{CrO}_3$  ( $0 \leq x \leq 0.5$ ) powders.

$\text{La}_{1-x}\text{Ca}_x\text{CrO}_3$	Lattice parameters			Cell volume ( $\text{\AA}^3$ )	wRp	Rp
	a( $\text{\AA}$ )	b( $\text{\AA}$ )	c( $\text{\AA}$ )			
x=0	5.482	7.762	5.518	234.774	0.16	0.13
x=0.1	5.471	7.743	5.499	232.981	0.16	0.13
x=0.2	5.452	7.712	5.475	230.219	0.14	0.11
x=0.3	5.437	7.682	5.491	229.352	0.17	0.14
x=0.4	5.428	7.668	5.484	228.274	0.16	0.14
x=0.5	5.414	7.667	5.410	224.579	0.20	0.15

The SEM images in Fig. 3 clearly show the microstructure of the  $\text{La}_{1-x}\text{Ca}_x\text{CrO}_3$  system, which it can be seen that the oxides are composed of nearly spherical particles and the average particle size increases with Ca content. This seems to be indicative of an incorporation of Ca into La-sites, thereby promoting grain growth and increasing the free energy of the system.<sup>44</sup> What is more, the few isolated pores that are visible are sufficient to produce “light traps” that are capable of scattering light at different angles through a combination of reflection, refraction, and scattering. This ultimately increases the optical path of the oxide, and therefore improves its spectral absorption. Wen et al. have suggested that there is a certain correlation between emissivity and surface roughness;<sup>45</sup> other studies have confirmed this.<sup>46,47</sup> Thus, in order to study the surface condition of each sample, their surface roughness ( $R_a$ ) was determined by using a 3D laser microscope (OLS4000, Japan) to scan the surface.

Figure S2 shows the micrographs (greyscale) and surface roughness statistical graphs (colour) for each sample, from which we see that the  $\text{La}_{1-x}\text{Ca}_x\text{CrO}_3$  oxides ( $0 \leq x \leq 0.4$ ) have a very similar  $R_a$  of  $0.18 \mu\text{m}$ . From Fig.6, it is also evident that the absorption spectrum of  $\text{LaCrO}_3$  differs quite significantly from that of Ca-doped  $\text{LaCrO}_3$  ( $0.1 \leq x \leq 0.4$ ) across a range of different wavelengths. In contrast,  $\text{La}_{0.5}\text{Ca}_{0.5}\text{CrO}_3$  gives a much higher  $R_a$  of  $0.29 \mu\text{m}$  and a little higher absorbance; the increased surface roughness produced by excessive Ca doping has little effect on the absorption properties in the case of  $\text{La}_{0.5}\text{Ca}_{0.5}\text{CrO}_3$ . It can therefore be concluded that Ca doping can mainly affect the spectral properties.

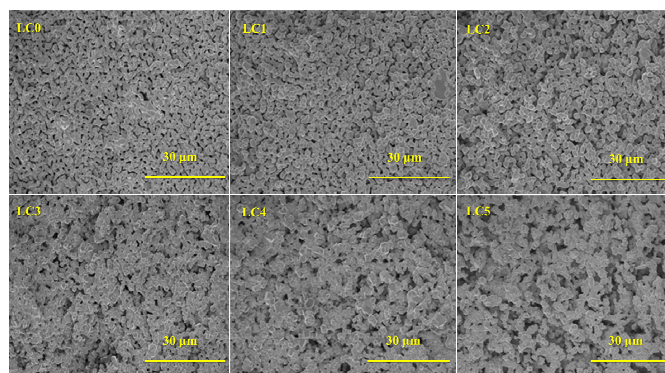


**Fig.3** SEM images of  $\text{La}_{1-x}\text{Ca}_x\text{CrO}_3$  ( $0 \leq x \leq 0.5$ ).

The FTIR spectrum of  $\text{La}_{1-x}\text{Ca}_x\text{CrO}_3$  in Fig. 4 reveals several main absorption peaks between  $400$  and  $4000 \text{ cm}^{-1}$ , with the absorption bands at  $449$ ,  $594$ , and  $636 \text{ cm}^{-1}$  assigned to the O-Cr-O, Cr-O, and Cr-O stretching mode vibrations, respectively. The higher frequency band extends from  $800$  to  $475 \text{ cm}^{-1}$  with a center of  $540 \text{ cm}^{-1}$  due to a stretching vibration, whereas the low frequency band extends from  $475$  to  $300 \text{ cm}^{-1}$  with a center of  $400 \text{ cm}^{-1}$  due to a bending vibration of metal oxygen bonds. Meanwhile, the weak peak at  $920 \text{ cm}^{-1}$  is attributed to the La-O stretching vibration.<sup>48-50</sup> The disappearance of the peaks at  $594 \text{ cm}^{-1}$  and  $636 \text{ cm}^{-1}$  with increasing  $\text{Ca}^{2+}$  concentration can therefore be explained by a change in the force constants and bond distances that cause lattice distortion. In the perovskite structure, the A-site cation is surrounded by twelve oxygen ions, whereas the B-site cation is bonded to six oxygen ions in the octahedral interstices of the oxygen sub-lattice. The vibrational modes associated with the motion of these atoms would therefore be expected to be sensitive to the force constants, and hence the bond distances.<sup>34</sup> When the oxide is irradiated by a certain frequency of infrared light its dipole moments increase or decrease in response to the forces acting on dipoles in the periodic field, and it is these vibrating dipole moments that cause infrared absorption.

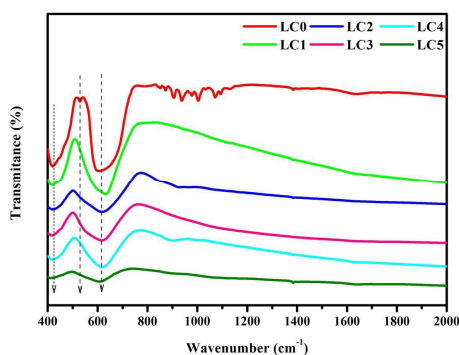


Fig.4 Infrared transmission spectra of  $\text{La}_{1-x}\text{Ca}_x\text{CrO}_3$  ( $0 \leq x \leq 0.5$ ).

### Surface composition

From the compositional surface analysis of each sample performed by X-ray photoelectron spectroscopy (XPS), the binding energies (Tab. 2) were determined from a best fit of the representative peaks for the La 3d, O1s, and Cr 2p levels. The fitted XPS spectra for the most relevant regions of the sample series ( $x = 0, 0.5$ ) are displayed in Fig. 5, which reveals that there is no significant difference between samples in the La 3d zone (Fig. 5a); all display the typical double-peak profile of La 3d<sub>3/2</sub> at around 854.7 and 850.9 eV, with La 3d<sub>5/2</sub> components at around 834.1 and 837.8 eV. Interestingly, these energies are all quite close to the values recorded for La<sup>3+</sup> ions in an oxidizing environment.<sup>51</sup> In the O1s zone (Fig. 5b), there are two main peaks clearly discernible: a low-binding-energy peak at around 529.0 eV that is typically attributed to lattice oxide species, and a broader peak at around 531.2 eV that can be attributed to CO<sub>3</sub><sup>2-</sup>, OH<sup>-</sup>, O<sup>-</sup>, O<sub>2</sub><sup>2-</sup>, and O<sup>2-</sup> species adsorbed on the surface.<sup>52</sup> Note also that as the concentration of Ca is increased, the peak corresponding to lattice oxygen (O<sup>2-</sup>) disappears, which indicates the formation of oxygen vacancies. In the Cr 2p spectra (Fig. 5c), the undoped  $\text{La}_{1-x}\text{Ca}_x\text{CrO}_3$  ( $x = 0$ ) system exhibits a clear peak at about 576 eV (Cr<sup>3+</sup>/Cr<sup>4+</sup>), with no peak being detected around 579 eV (Cr<sup>6+</sup>).<sup>53</sup> However, as the concentration of Ca is increased, the appearance of a peak at around 579 eV is indicative of an increase in Cr<sup>6+</sup> concentration to maintain electrical neutrality. This increase in Cr<sup>6+</sup> ions in turn leads to the generation of more oxygen vacancies, as evidenced by the ratio of absorbed oxygen in the O 1s zone. This is significant, as the oxidation state of Cr and O ions has an effect on the solar absorption properties of the  $\text{La}_{1-x}\text{Ca}_x\text{CrO}_3$  system.

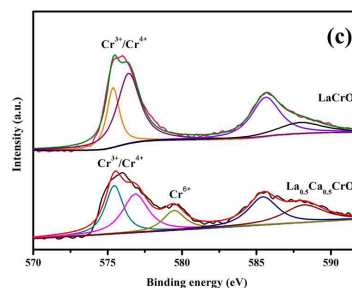
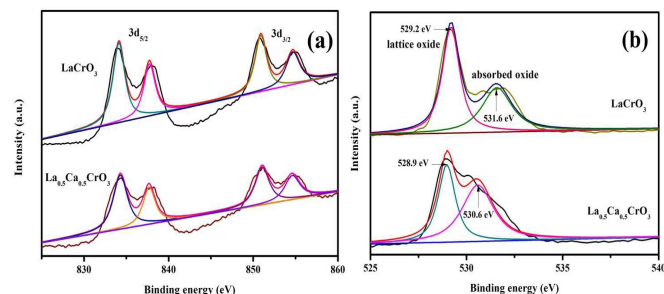


Fig. 5 X-ray photoelectron spectra of (a) La 3d, (b) O 1s, and (c) Cr 2p of  $\text{La}_{1-x}\text{Ca}_x\text{CrO}_3$  ( $x = 0, 0.5$ )

Tab.2 Binding energies of the main peaks of core electrons, as extracted from the XPS spectra of  $\text{La}_{1-x}\text{Ca}_x\text{CrO}_3$  ( $x = 0, 0.5$ ).

Sample	XPS binding energy (eV) of main peaks (relative percentage in parenthesis)		
	La 3d <sub>5/2</sub>	O 1s	Cr 2p <sub>3/2</sub>
LaCrO <sub>3</sub>	834.1	529.2 (58.2)	575.4 (67.9)
	837.8	531.6 (41.8)	576.4 (32.1)
La <sub>0.5</sub> Ca <sub>0.5</sub> CrO <sub>3</sub>	834.3	528.9 (39.5)	575.4 (37.9)
	837.7	530.6 (60.5)	576.9 (43.0)

### Diffused spectrum and thermal properties

In Fig. 6, it can be seen that the absorption spectra of  $\text{LaCrO}_3$  differs quite significantly from that of Ca-doped  $\text{LaCrO}_3$  across a range of different wavelengths. From the calculated values of  $\alpha_s$  and  $\epsilon$  displayed in Tab. 3 it is clear that Ca doping enhances both the solar absorption and thermal emission, with both reaching an equilibrium value at  $x = 0.2$  of as much as 95 % and 0.94, respectively. The mixed oxide created upon substitution of La with an alkaline earth metal induces the generation of Cr<sup>4+</sup> or Cr<sup>6+</sup> species,<sup>54-56</sup> which means that Ca<sup>2+</sup> doping introduces an impurity energy level of Cr<sup>4+</sup> in the  $\text{LaCrO}_3$  forbidden gap. This generates Cr<sup>3+</sup>-O-Cr<sup>4+</sup> polar hopping with an activation energy of 0.32 eV and an optical band gap of 2.15 eV, as per the de Broglie Relation:

$$\lambda = \frac{hc}{E_a}$$

where  $h = 6.62606896 \times 10^{-34}$  J·s,  $c$  is the speed of light, and  $E_a$  is the activation energy. From this, the maximum excitation wavelength of  $\text{LaCrO}_3$  and Cr<sup>3+</sup>-O-Cr<sup>4+</sup> polar hopping are calculated to be 0.576 and 3.874  $\mu\text{m}$ , respectively,<sup>57,58</sup> from which it can be concluded that Ca<sup>2+</sup> doping broadens the scope of spectral absorption.

The law of conservation of energy rules that the amount of incident energy must be equal to the sum of the absorbed, reflected and transmitted energy for an object in a vacuum at constant temperature. In other words, as there is no other source of energy input or output, any energy absorbed by an object must increase its thermal energy; so in order for the temperature of the object to remain constant, it must radiate the same amount of energy as it absorbs. A perfect emitter is therefore

also a perfect absorber, and by this analogy, those samples with a higher absorbance in the infrared spectrum can be assumed to have better thermal radiation properties. From Fig. 5 and Fig. 8, we see that Ca-doped  $\text{LaCrO}_3$  exhibits a higher infrared absorbance than  $\text{LaCrO}_3$ . This clearly demonstrates that doping can alter the optical energy band and influence the spectral properties of a material,<sup>59-62</sup> which in the case of  $\text{Ca}^{2+}$  doping, is due to an introduction of an impurity energy level of  $\text{Cr}^{4+}$  or  $\text{Cr}^{6+}$  in the  $\text{LaCrO}_3$  forbidden gap.

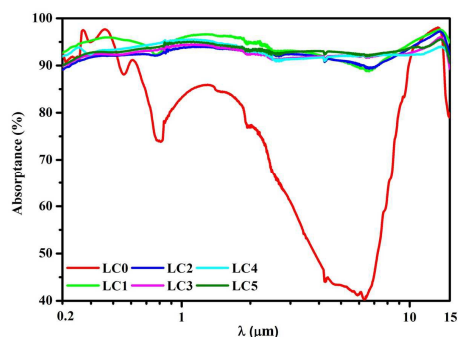


**Fig.6** Room temperature absorption spectra in the 0.2–15  $\mu\text{m}$  wavelength range for  $\text{La}_{1-x}\text{Ca}_x\text{CrO}_3$  ( $0 \leq x \leq 0.5$ )

**Tab.3** Solar absorptivity and infrared emissivity of the  $\text{La}_{1-x}\text{Ca}_x\text{CrO}_3$  system

Spectral region ( $\mu\text{m}$ )	0.2–3	3–5	8–14	2.5–15
	Solar absorption ( $\alpha$ )	Infrared emissivity ( $\epsilon$ )		
$\text{LaCrO}_3$	77.4 %	0.46	0.89	0.72
$\text{La}_{0.9}\text{Ca}_{0.1}\text{CrO}_3$	91.7 %	0.92	0.95	0.93
$\text{La}_{0.8}\text{Ca}_{0.2}\text{CrO}_3$	94.0 %	0.92	0.94	0.93
$\text{La}_{0.7}\text{Ca}_{0.3}\text{CrO}_3$	93.8 %	0.92	0.93	0.93
$\text{La}_{0.6}\text{Ca}_{0.4}\text{CrO}_3$	93.9 %	0.92	0.93	0.92
$\text{La}_{0.5}\text{Ca}_{0.5}\text{CrO}_3$	94.5 %	0.93	0.94	0.94

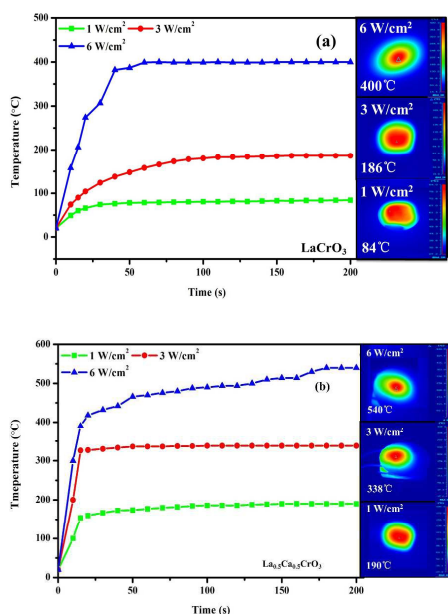


**Fig.7** Temperature dependence of radiative heating time for (a)  $\text{LaCrO}_3$  and (b)  $\text{La}_{0.5}\text{Ca}_{0.5}\text{CrO}_3$ .

In order to better illustrate the high solar absorbance created by Ca doping, the thermal irradiation performance of LC0 and LC5 was investigated further by recording their irradiation temperature for a given mass under a concentrated light source at different time intervals. As shown in Fig. 8, the temperature of the LC0 was found to initially increase rapidly with solar intensity, but reached a plateau within the first 50 s; the equilibrium value increasing only with the intensity of irradiation, not duration. In comparison, LC5 reached a steady-state condition more quickly and had a higher equilibrium value for any given intensity, and so clearly has the better solar absorption and thermal irradiation properties when used as a light absorber.

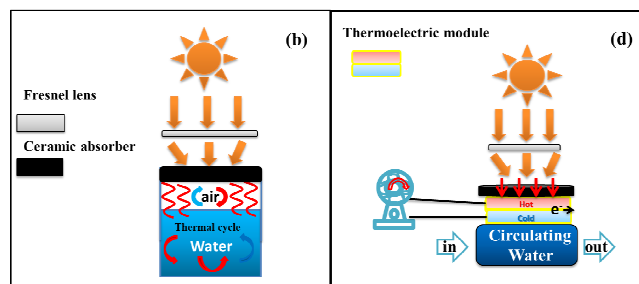
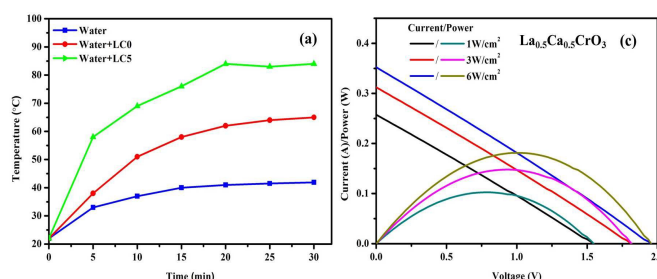


**Fig.8** (a) Temperature dependence of radiative heating time for water using  $\text{LaCrO}_3$  and  $\text{La}_{0.5}\text{Ca}_{0.5}\text{CrO}_3$  as source of radiation under a solar intensity of  $3 \text{ W/cm}^2$ . (c) Current-voltage and power-voltage curves of the device under irradiation at various incident fluxes for  $\text{La}_{0.5}\text{Ca}_{0.5}\text{CrO}_3$ . (b,d) Schematic diagrams showing the self-assembly of a solar thermal measurement device.

Figure 8 gives an example of the practical application of LC5 in the solar thermal radiation field. For this, its thermal expansion ( $\Delta L/L_0$ ) and coefficient of thermal expansion were measured in air between 50 and 500  $^\circ\text{C}$ ; the latter giving a value of  $11.2 \times 10^{-6} / ^\circ\text{C}$  that indicates sufficient thermal stability to meet basic application needs. It is known that the infrared absorbance of LC5 is enhanced with increasing temperature in Fig. 9. According to Kirchhoff's law and the law of energy conservation, infrared emissivity of opaque materials is equal to their absorbance. Thus, LC5 has the highest infrared emissivity at 400  $^\circ\text{C}$ , which is consistent with the observation of samples irradiated under a solar intensity of  $3 \text{ W/cm}^2$ .

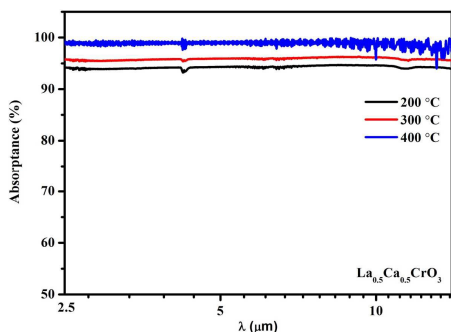


Fig. 9 Temperature dependence of the absorption spectra in the 2.5–15  $\mu\text{m}$  wavelength range for  $\text{La}_{0.5}\text{Ca}_{0.5}\text{CrO}_3$ .

The experimental device used for heating water show in Fig. 8b consisted of an optical concentration system, a ceramic radiator (LC5) and water. Since pure water absorbs almost all solar energy in the near infrared and infrared spectrum, but little in the visible range, its volume ( $6 \times 10^{-5} \text{ m}^3$ ) causes a  $\sim 15^\circ\text{C}$  temperature rise under steady-state conditions. Thus, in the case of LC5 ( $2.8 \times 10^{-3} \text{ m}^2$  irradiative area, 10 g), the temperature of the water increases to  $84^\circ\text{C}$  within 30 min, as illustrated in Fig. 8a. More interesting, however, is the fact that LC5 can also utilize the heat generated by coupling it to a thermoelectric module to produce electricity. As seen in Fig. 7d, the thermoelectric module was sandwiched between the LC5 and a custom-made water cooling system that was used to increase the temperature difference across the thermoelectric module. The current-voltage and power-voltage curves in Fig. 8c reveal both the open circuit voltage and short-circuit current increase with incident flux. Moreover, the near-linear relationship between current and voltage implies that the voltage generated is constant.<sup>63</sup> The peak output power ( $P_{\text{max}}$ ) was calculated to be 0.18 W for an incident flux of  $6 \text{ W}/\text{cm}^2$ , which is sufficient output to easily drive a propeller motor (see the video provided in the Supporting Information) and is comparable to the effect recently achieved by  $\text{Sm}_{0.5}\text{Sr}_{0.5}\text{CoO}_{3-\delta}$  light absorbers.<sup>64</sup> Since  $\text{La}_{0.5}\text{Ca}_{0.5}\text{CrO}_3$  offers the best combination of solar absorption and thermal emittance, it is considered to have great potential for use in solar thermal radiation applications.

## Conclusions

A series of Ca-doped lanthanum chromites,  $\text{La}_{1-x}\text{Ca}_x\text{CrO}_3$  ( $0 \leq x \leq 0.5$ ), were successfully synthesized by a traditional solid state reaction, with subsequent TG-DSC and XRD analysis identifying  $1400^\circ\text{C}$  as an appropriate sintering temperature. XRD and FTIR analysis confirmed that Ca ions are doped into  $\text{LaCrO}_3$ , with the tolerance factor and cell parameters revealing a greater distortion of the crystal lattice with increasing dopant concentration. XPS analysis also identified that the chromium ions are in a mixed valence state, with the ratio of  $\text{Cr}^{3+}$  to  $\text{Cr}^{6+}$  decreasing with  $\text{Ca}^{2+}$  concentration. The porous surface morphology of the samples, as observed by SEM, also creates “light traps” that increase the optical path and absorption of sunlight. Calculation of the solar absorbance and infrared emissivity demonstrated that Ca doping broadens the spectral

absorption of  $\text{LaCrO}_3$  oxides; the optimal composition of  $\text{La}_{0.5}\text{Ca}_{0.5}\text{CrO}_3$  exhibiting an excellent solar absorption of 95 % and a thermal irradiation of 0.94. Moreover, as the infrared emission increases with temperature, using this material as a light absorber allows for both the generation of electricity and heating of water. On the basis of these findings, Ca-doped lanthanum chromites are expected to become an important energy-saving material in high temperature applications.

## Acknowledgements

This work was supported by the funding from the Priority Academic Program Development of the Jiangsu Higher Education Institutions (PAPD), the Innovation Foundation for Graduate Students of Jiangsu Province (KYLX\_0745), the Innovation Foundation for Graduate Students of Jiangsu Province (CXZZ13\_0425), the independent research topic of State Key Laboratory of Materials-Oriented Chemical Engineering (ZK201211), as well as the Key Laboratory of Inorganic Coating Materials, Chinese Academy of Sciences (KLICM-2014-10).

## Notes

<sup>a</sup> State Key Laboratory of Materials-Oriented Chemical Engineering, College of Materials Science and Engineering, Nanjing Tech University, Nanjing 210009, P. R. China

<sup>b</sup> Key Laboratory of Inorganic Coating Materials, Chinese Academy of Sciences, Shanghai 200050, PR China

† Corresponding author. Tel.: +86 25 83587252, fax: +86 25 83587220 (C. Lu); Tel. / fax: +86 25 83172128 (Z. Xu). Email address: [chhu@njtech.edu.cn](mailto:chhu@njtech.edu.cn) (C. Lu), [zzxu@njtech.edu.cn](mailto:zzxu@njtech.edu.cn) (Z. Xu).

## References

- W. Jaspreet, D. Navneet, F. Jeremy, K. Iman, F. James, L. Ray and S.S. Simarjeet, *Nano Lett.*, 2014, **10**, 5820-5826.
- D. Tulchinsky, V. Uvarov, I. Popov, D. Mandler and S. Magdassi, *Sol. Energy Mater. Sol. Cells*, 2014, **120**, 23-29.
- L.L. Baranowski, G.J. Snyder and E.S. Toberer, *Energy Environ. Sci.*, 2012, **5**, 9055-9067.
- M. Roeb and H. Muller-Steinhagen, *Sci.*, 2010, **329**, 773-774.
- P.K. Jain, X.H. Huang, I.H. El-sayed and M.A. El-sayed, *Accounts Chem. Res.*, 2008, **41**, 1578-1586.
- H. Sai, H. Yugami, Y. Kanamori and K. Hane, *Sol. Energy Mater. Sol. Cells*, 2003, **79**, 35-49.
- Z.R. Abrams, M. Gharghi, A. Niv, C. Gladden and X. Zhang, *Sol. Energy Mater. Sol. Cells*, 2012, **99**, 308-315.
- J. Bisquert, D. Cahen, G. Hodes, S. Rühle and A. Zaban, *J. Phys. Chem. B*, 2014, **108**, 8106-8118.
- A. Goetzberger and C. Hebling, *Sol. Energy Mater. Sol. Cells* 2000, **62**, 1-9.
- O.P. Agnihotri and B.K. Gupta, *Solar Selective Surfaces Wiley-Interscience*, New York, 1981.
- E. Sani, L. Mercatelli, F. Francini, J.L. Sans and D. Sciti, *Scripta Mater.*, 2011, **65**, 775-778.
- B. Pierrat, M. Balat-Pichelin, L. Silvestroni and D. Sciti, *Sol. Energy Mater. Sol. Cells*, 2011, **95**, 2228-2237.

- 13 E. Sani, L. Mercatelli, P. Sansoni, L. Silvestroni and D. Sciti, *J. Renewable Sustainable Energy*, 2012, **4**, 033104.
- 14 D. Sciti and L. Silvestroni, *J. Eur. Ceram. Soc.*, 2012, **32**, 1933-1940.
- 15 D. Sciti, L. Silvestroni, L. Mercatelli, J.L. Sans and E. Sani, *Sol. Energy Mater. Sol. Cells*, 2013, **109**, 8-16.
- 16 X.D. He, Y.B. Li, L.D. Wang, Y. Sun and S. Zhang, *J. Am. Ceram. Soc.*, 2011, **94**, 3195-3197.
- 17 Benkő I, *Int. J. Global Energy Issues*, 2002, **17**, 60-67.
- 18 Dahan N., Niv A., Biener G., Y. Gorodetski, V. Kleiner and E. Hasman, *J. Heat Transf.*, 2008, **130**, 112401-112405.
- 19 W.F. Bogaerts and C.M. Lampert, *J. Mater. Sci.*, 1983, **18**, 2847-2875.
- 20 C.E. Kennedy, National Renewable Energy Laboratory 1617 Cole Blvd. Golden, CO 80401-3393, NREL/TP-520-31267, 2002.
- 21 J.J. Neumeier and H. Terashita, *Phys. Rev. B*, 2004, **70**, 214435-214437.
- 22 P. Duran, J. Tartaj, F. Capel and C. Moure, *J. Eur. Ceram. Soc.*, 2004, **24**, 2619-2629.
- 23 G.A. Tompsett and N.M. Sammes, *J. Power Sources*, 2004, **130**, 1-7.
- 24 K. Hilpert, R.W. Steinbrech, F. Boroomand, E. Wessel, F. Meschke, A. Zuev, O. Teller, H. Nickel and L. Singheiser, *J. Eur. Ceram. Soc.*, 2003, **23**, 3009-3020.
- 25 F. Riffard, J. Fondard, P. Moulin, S. Perrier and H. Buscail, *Oxid. Met.*, 2014, **81**, 191-201.
- 26 C. Solís, L. Navarrete, M. Balaguer and J.M. Serra, *J. Power Sources*, 2014, **258**, 98-107.
- 27 Y.Z. Jiang, J.F. Gao, M.F. Liu, Y.Y. Wang and G.Y. Meng, *Mater. Lett.*, 2007, **61**, 1908-1911.
- 28 L.P. Rivas-Vázquez, J.C. Rendón-Angeles, J.L. Rodríguez-Galicia, C.A. Gutiérrez-Chavarría, K.J. Zhu and K. Yanagisawa, *J. Eur. Ceram. Soc.*, 2006, **26**, 81-88.
- 29 D.E.P. Vanpoucke, P. Bultinck, S. Cottenier, V.V. Speybroeck, I.V. Driessche, *J. Mater. Chem. A*, 2014, **2**, 13723-13737.
- 30 B. Singh, S.Y. Jeon, J.H. Kim, J.Y. Park, C. Baed and S.J. Song, *J. Electrochem. Soc.*, 2014, **161**, F464-F472.
- 31 S. Lee and C.A. Randall, *Solid State Ionics*, 2013, **249**, 86-92.
- 32 V.A. Khomchenko and J.A. Paixão, *J. Appl. Phys.*, 2014, **116**, 214105.
- 33 M. Mori, T. Yamamoto, H. Itoh and T. Watanabe, *Mater. Sci.*, 1997, **32**, 2423-2431.
- 34 S. Mukherjee, M.R. Gonal, M.K. Patel, M. Roy, A. Patra and A.K. Tyagi, *J. Am. Ceram. Soc.* 2012, **95**, 290-295.
- 35 S.P. Jiang, L. Liu, K.P. Ong, P. Wu, J. Li, and J. Pu, *J. Power Sources*, 2008, **176**, 82-89.
- 36 A.C. Larson and R.B.V. Dreele, *National Laboratory Report LAUR.*, 1994, 86-748.
- 37 B. Toby, *J. Appl. Crystallogr.*, 2001, **34**, 210-213.
- 38 Y. Mastai, S. Polarz and M. Antonietti, *Adv. Funct. Mater.*, 2002, **12**, 197-202.
- 39 X.D. Xiao, L. Miao, G. Xu, L.M. Lu, Z.M. Su and N. Wang, *Appl. Surf. Sci.*, 2011, **257**, 10729-10736.
- 40 A. Orera, G. Larraz and M.L. Sanjuán, *J. Eur. Ceram. Soc.*, 2013, **33**, 2103-2110.
- 41 R.L. Frost and M. Weier, *Thermochim. Acta*, 2003, **406**, 221-232.
- 42 R.D. Shannon, *Acta Cryst. A.*, 1976, **32**, 751-767.
- 43 H. Bhatt, J. Bahadur, M.N. Deo, S. Ramanathan, K.K. Pandey, D. Sen, S. Mazumder and S.M. Sharma, *J. Solid State Chem.*, 2011, **184**, 204-213.
- 44 J.H. Cheng and A. Navrotsky, *J. Solid State Chem.*, 2005, **178**, 234-44.
- 45 C.D. Wen and I. Mudawar, *Int. J. Heat Mass Transf.*, 2006, **49**, 4279-4289.
- 46 L. Yuan, X.L. Weng, W.F. Du, J.L. Xie and L.J. Deng, *J. Alloys Compd.*, 2014, **583**, 492-497.
- 47 F.Y. Wang, L.F. Cheng, H. Mei, Q. Zhang and L. Zhang, *Int. J. Thermophys.*, 2014, **35**, 62-75.
- 48 P. Kumar, R.K. Singh, A.S.K. Sinha and P. Singh, *J. Alloys Compd.*, 2013, **576**, 154-160.
- 49 A.A. Athawale and P.A. Desai, *Ceram. Int.*, 2011, **37**, 3037-3043.
- 50 K. Rida, A. Benabbas, F. Bouremmad, M.A. Peña and E. Sastre, *Appl. Catal. A-general*, 2007, **327**, 173-179.
- 51 Y. Uwamino, T. Ishizuka and H. Yamatera, *J. Electron Spectrosc. Rel. Phenom.*, 1984, **34**, 67-78.
- 52 S. Ponce, M.A. Peña and J.L.G. Fierro, *Appl. Catal. B*, 2000, **24**, 193-205.
- 53 Y.Z. Jiang, J.F. Gao, M.F. Liu, Y.Y. Wang and G.Y. Meng, *Mater. Lett.*, 2007, **61**, 1908-1911.
- 54 X.M. Liu, W.H. Su and Z. Lu, *J. Phys. Chem. Solids*, 2001, **62**, 1919-1921.
- 55 N. Sakai, T. Tsunoda, N. Fukumoto, I. Kojima, K. Yamaji, T. Horita, M. Ishikawa, H. Yokokawa and M. Dokiya, *J. Electroceram.*, 1999, **4**, 121-128.
- 56 K. Rida, A. Benabbas, F. Bouremmad, M.A. Peña and A. Martínez-Arias, *Catal. Commun.*, 2006, **7**, 963-968.
- 57 D.C. Look, S. Chaudhuri and L. Eaves, *Phys. Rev. Lett.*, 1982, **49**, 1728-1731.
- 58 K.P. Ong, P. Blaha and Wu P., *Phys. Rev. B.*, 2008, **77**, 073102-073106.
- 59 S. Shailajha, K. Geetha, P. Vasantharani and S.A. Kadhar, *Spectrochim. Acta, Part A*, 2015, **138**, 846-856.
- 60 K. Vijayalakshmi and S.D. Jereil, *Ceram. Int.*, 2015, **41**, 3220-3226.
- 61 B.S. Ko, S.J. Lee and D.H. Kim, *J. Nanosci. Nanotechnol.*, 2015, **15**, 2432-2435.
- 62 G. Turgut, E.F. Keskenler, S. Aydin, M. Yılmaz, S. Doğan and B. Düzgün, *Phys. Scr.*, 2013, **87**, 035602.
- 63 Y.Q. Chen, K.W. Chen, H. Bai and L. Li, *Mater. Chem.*, 2012, **22**, 17800-17804.
- 64 Z.G. Fang, C.H. Lu, D.S. Gao, Y. Lu, C.P. Guo, Y.R. Ni, Z.Z. Xu and P.W. Li, *J. Eur. Ceram. Soc.*, 2015, **35**, 1343-1348.